Journal of Power Sources 195 (2010) 8258–8266

Contents lists available at ScienceDirect

Journal of Power Sources

journal homepage: www.elsevier.com/locate/jpowsour

Structural changes in a commercial lithium-ion battery during electrochemical cycling: An *in situ* neutron diffraction study

Neeraj Sharma[a,*], Vanessa K. Peterson[a], Margaret M. Elcombe[a], Maxim Avdeev[a], Andrew J. Studer[a], Ned Blagojevic[b], Rozila Yusoff[c], Norlida Kamarulzaman[c]

[a] *Bragg Institute, Australian Nuclear Science and Technology Organisation, Locked Bag 2001, Kirrawee DC, NSW 2232, Australia*
[b] *Institute of Materials Engineering, Australian Nuclear Science and Technology Organisation, Locked Bag 2001, Kirrawee DC, NSW 2232, Australia*
[c] *Centre for Nanomaterials Research, Institute of Science, Faculty of Applied Sciences, Universiti Technologi MARA, 40450 Shah Alam, Selangor, Malaysia*

ARTICLE INFO

Article history:
Received 21 April 2010
Received in revised form 25 June 2010
Accepted 30 June 2010
Available online 21 July 2010

Keywords:
In situ neutron diffraction
Lithium-ion battery
Graphite
Lithium cobalt oxide
Structural change

ABSTRACT

The structural response to electrochemical cycling of the components within a commercial Li-ion battery ($LiCoO_2$ cathode, graphite anode) is shown through *in situ* neutron diffraction. Lithuim insertion and extraction is observed in both the cathode and anode. In particular, reversible Li incorporation into both layered and spinel-type $LiCoO_2$ phases that comprise the cathode is shown and each of these components features several phase transitions attributed to Li content and correlated with the state-of-charge of the battery. At the anode, a constant cell voltage correlates with a stable lithiated graphite phase. Transformation to de-lithiated graphite at the discharged state is characterised by a sharp decrease in both structural cell parameters and cell voltage. In the charged state, a two-phase region exists and is composed of the lithiated graphite phase and about 64% LiC_6. It is postulated that trapping Li in the solid|electrolyte interface layer results in minimal structural changes to the lithiated graphite anode across the constant cell voltage regions of the electrochemical cycle.

1. Introduction

Secondary Li-ion batteries, commercialised by the Sony Corporation in 1991 [1,2], are composed of a graphite anode and a $LiCoO_2$ cathode. The cell produces an output of 3.6 V, *i.e.*, about three times higher than conventional alkaline batteries. During charging and discharging, these Li-ion batteries function through insertion and extraction of Li-ions to and from the electrodes *via* a non-aqueous electrolyte. Lithium-ion batteries have gained widespread use due to their high capacity levels, high specific energy, high power rates, and low self-discharge with good cycle-life [3,4]. The increasing demand for these batteries for applications that require higher voltages, better cycling and increased safety has driven their improvement, through a variety of approaches that include cathode doping [3] and replacement of non-aqueous liquid electrolytes with solid polymers [5].

There is a significant amount of work aimed at understanding the structure of the electrode materials both before and after cycling, *e.g.*, see [1]. Usually the crystal structure of electrode materials can only be correlated with a particular state-of-charge *ex situ*, once the component of interest has been extracted from the battery, *e.g.*, Ref. [6]. This method gives no insight into ongoing processes, and is complicated by self-discharge effects, effects from interaction of certain components with air during the extraction process, and Li loss. A more comprehensive insight into structural processes can be gained by using *in situ* studies of electrode structure as a function of the electrochemical cycle. Such work reveals insights into the mechanism of battery functionality that can be used to direct improvements in battery performance through modifications of component crystal structures or electrochemical cycling factors.

In situ X-ray diffraction (XRD) has been used to assist the understanding of the lattice parameter changes of cathode materials [7–20]. Changes in cathode lattice parameters are directly related to the Li insertion/extraction processes. For example, removing Li-ions from $LiCoO_2$ causes the negatively charged CoO_2 layers composed of edge-sharing CoO_6 octahedra to repel each other and thereby cause an increase in the *c*-axis lattice parameter [3]. In general, *in situ* XRD experiments are performed using a specially designed cell that resembles a coin (coin cell) and contains a Li anode to probe changes in the cathode structure. Unfortunately the mechanism of X-ray scattering from a sample results in a limited penetration depth of the X-rays into the sample and therefore analysis of only a relatively small proportion of the sample, close to the surface is possible. X-rays also have a limited ability to detect

* Corresponding author. Tel.: +61 2 9717 7253; fax: +61 2 9717 3606.
E-mail addresses: Neeraj.Sharma@ansto.gov.au, njs@ansto.gov.au (N. Sharma).

0378-7753/$ – see front matter © 2010 Elsevier B.V. All rights reserved.
doi:10.1016/j.jpowsour.2010.06.114

Li, particularly in the presence of heavier elements, due to its low scattering power. As a consequence of these limitations, *in situ* XRD studies of Li batteries have revealed information restricted to the surface structure, evolution of structural cell parameters, and phase fractions of one component [7,21,22].

In situ neutron diffraction (ND) has been applied to Li batteries [23–27] and overcomes many of the difficulties of X-ray based techniques. Neutrons interact predominantly with the nucleus of atoms, enabling further penetration into the material(s) of interest and allowing both anode and cathode structure to be simultaneously investigated. ND is more sensitive than XRD to Li, particularly in the presence of elements with a much larger number of electrons, such as Co. *In situ* ND is used to determine lattice parameters, phase fractions, and detailed structural information such as Li position and content in the anode and cathode materials. The usefulness of *in situ* ND for the analysis of battery materials is well-demonstrated by studies of nickel–metal-hydride batteries, where neutrons are particularly sensitive to the isotope of hydrogen, deuterium (D) [28,29]. *In situ* ND studies of Li batteries have used either a coin cell configuration [23] with $LiNiO_2$ cathodes, or specially designed cylindrical cells [24,25] with $LiMn_2O_4$ cathodes. To date, two studies [26,27] have investigated commercially available batteries (*e.g.*, $LiCoO_2$ and $LiFePO_4$ cathodes with graphite anodes) and attempted to track changes in components other than cathodes. A study on $LiCoO_2$ only presented information on a relatively small range of interplanar spacings (d) in the crystal lattice ($1.3 \leq d \leq 1.75$ Å) at about seven points during discharge. They observed five reflections of the phases present in the battery that were sufficient to show the expansion of the c-axis of $LiCoO_2$ and graphite [26].

In situ ND experiments on Li-ion batteries are challenging, and the relatively few publications reflect these challenges rather than the usefulness of the technique. Perhaps the major challenge in these experiments is the large neutron scattering cross-section of hydrogen, an element commonly found in the electrolyte and polymer separator components of these batteries. The dominant portion of this scattering is incoherent and isotropic, and results in a large contribution to the background, significantly reducing the signal-to-noise ratio in structural studies. This problem can be mitigated by substituting hydrogen with deuterium, which has a far smaller incoherent neutron scattering cross-section. Whilst the substitution is relatively straightforward, the cost of deuterated components can be prohibitive. Other considerations in conducting a successful *in situ* neutron diffraction experiment include angular range and resolution, counting statistics (speed), and sample geometry. These factors are considered in the present work and experiments have been undertaken on a battery with sufficiently large electrode contents to give relatively intense Bragg peaks, and with its orientation optimised with respect to the signal-to-noise produced from the inhomogeneous cell.

This investigation presents a detailed structural study using *in situ* ND data from a commercially available Li-ion battery. The experiments collect real-time data (5 min acquisitions) over the d-spacing range of $1.35 \leq d \leq 6.28$ Å during charge–discharge cycles. The goals are: (i) to identify the phases present in the battery at various stages of the electrochemical cycle; (ii) to track the phase evolution over time and charge–discharge; (iii) to relate the crystal structure of components to electrochemical features such as the loss of charge. The interplay between bulk structural features of all components in the battery and the electrochemistry is presented. Finally, methods to improve future *in situ* ND studies are proposed.

2. Experimental

A commercial, prismatic Li-ion battery was obtained from CLEON Technologies Sdn Bhd, Malaysia and had dimensions of 45 mm × 45 mm × 5 mm. The cell consisted of a graphite anode, a $LiCoO_2$ cathode, a polymeric binder and carbon black, a $LiPF_6$ in organic carbonate (ethylene carbonate/diethylcarbonate) electrolyte, a Celgard® separator, and Copper current-collectors. These components are encased in a polymeric seal. ND experiments probe the ~4th to 5th electrochemical cycle of the as-purchased cell.

Neutron diffraction data were collected on the high-intensity powder diffractometer, Wombat, at the Open Pool Australian Lightwater (OPAL) reactor facility at the Australian Nuclear Science and Technology Organisation (ANSTO) [30]. The battery was placed in a $\lambda = 2.41$ Å neutron beam and patterns were collected every 5 min for 59 h in the two theta (2θ) range $16^\circ \leq 2\theta \leq 136^\circ$. Wombat features an area detector covering 120° in 2θ, enabling diffraction data to be continuously collected rather than a 2θ-step-scan type acquisition. Along with its relatively intense neutron beam, Wombat is an ideal instrument for *in situ* ND studies of the type performed here. Vertical focussing of the monochromator was used to increase further the intensity of the neutron beam on the sample. A significant sample geometry effect was noted, and arose from the different pathlengths of the incident and scattered neutrons within the sample. The sample orientation was optimised to give good data in the 2θ regions of interest. During data collection, the battery was electrochemically cycled in the galvanostatic (constant current) mode with applied currents of ±70 mA using a Solartron 1480 battery tester (the cell was not in equilibrium). Data correction, reduction and visualisation were undertaken using the program LAMP [31]. Rietveld refinements were carried out using the GSAS [32] suite of programs with the EXPGUI [33] interface.

3. Results and discussion

3.1. Total cell

Significant changes in the ND data during the electrochemical cycling are noted (Fig. 1(a)). An ND pattern of the as-received cell after the first 5 min of discharge is shown in Fig. 1(b). The feature (dip) at approximately $2\theta = 78^\circ$ arises from the increased path length of the neutrons travelling through the long axis of the battery. A broad background contribution is noted from the incoherent neutron scattering of hydrogen present in: (i) the organic hydrogen-rich electrolyte and separator, and (ii) the electrolyte solution. Phase identification for each reflection was undertaken by systematically considering the possibilities of phases known to exist in each component of the battery (*e.g.*, Co_3O_4 [34], CoO_2 [35], LT-$LiCoO_2$ [36–39] and HT-$LiCoO_2$ [40,41] for the cathode). Specifically, crystallographic information files (CIF) from the Inorganic Crystal Structure Database (ICSD) of each possible phase present in the sample were used to model the data using Rietveld refinement of only instrumental parameters (*e.g.*, peak shapes), scale factors, and lattice parameters. By this means, the major phases producing the observed reflections are identified as lithiated/de-lithiated graphite (stacked graphene layers), LiC_6, Cu, layered $Li_{1-x}CoO_2$, spinel-type Li_yCoO_2, and a broad contribution from carbon black. Reflections arising from these phases, with the exception of Cu and carbon black, varied with time during electrochemical cycling (Fig. 1(a)). These changes are described in the first part of this section, while details of the crystal structural changes to the phases, derived from Rietveld refinement of the structures of each phase, are discussed in Section 3.4.

3.2. Cathode

High-temperature $LiCoO_2$ (HT-$LiCoO_2$) or layered $LiCoO_2$ is a widely used cathode material consisting of a layered structure with $R\bar{3}m$ symmetry and $a = 2.816$ Å, $c = 14.08$ Å in the hexagonal setting [21]. This phase contains alternating planes of Li and Co

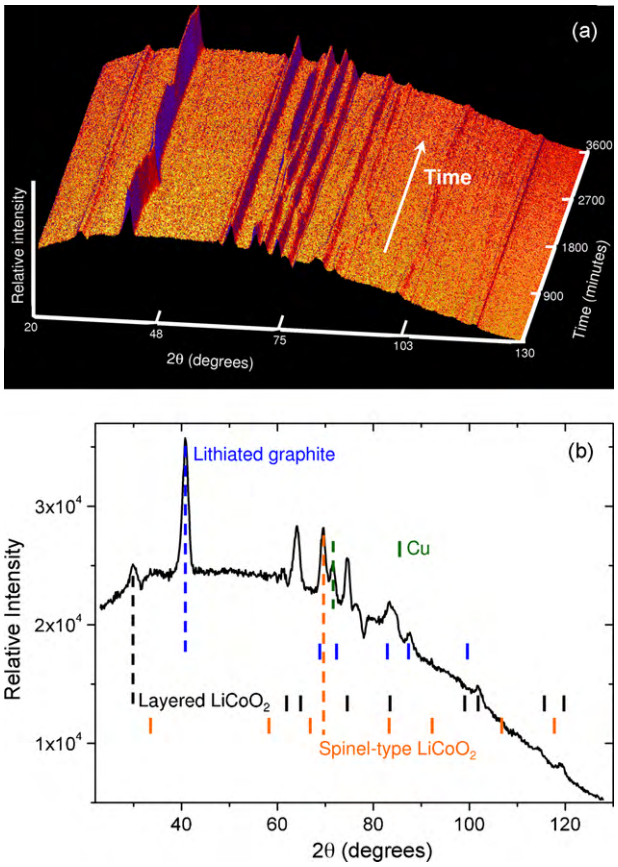

Fig. 1. (a) ND patterns collected as a function of time during electrochemical cycling showing changes in reflection intensity and position. Cell is discharged to 3.2 V at −70 mA, followed by charging to 4.2 V at 70 mA and final discharge at −70 mA. (b) First diffraction pattern collected after 5 min of discharging, with identified phases labelled with peak markers and key reflections in phase identification shown as dashed lines.

atoms separated by close-packed oxygen layers [21,42]. Lithium is extracted from these planes during charge and results in the repulsion of the negatively charged CoO_2 layers and an increase in the *c* lattice parameter. A low-temperature polymorph labelled LT-$LiCoO_2$ has been reported to adopt a '*quasi*-spinel structure' in cubic $Fd\bar{3}m$ symmetry. Differences between these phases arise from their synthesis temperatures, *e.g.*, 400 °C for LT-$LiCoO_2$ and 900 °C for HT-$LiCoO_2$, and result in different cation arrangements [36,37]. Since HT-$LiCoO_2$ has the higher thermodynamically stability, most commercial batteries contain HT-$LiCoO_2$ cathodes. LT-$LiCoO_2$, or a spinel version of $LiCoO_2$, is thought to contribute to capacity fading of these batteries with continual cycling [40,43–45]. Whether the capacity fading is due to the formation of LT-$LiCoO_2$ or another spinel-type phase remains unclear [44,45].

The presence of both layered and spinel-type structures in the $LiCoO_2$ cathode during charging/discharging is a key finding of this work. The HT-$LiCoO_2$ was modelled with Li and Co fully occupying 3*a* and 3*b* sites, respectively [38]. A spinel-type $LiCoO_2$ has also been identified using a starting structure from previous work [39]. In the Rietveld model for phase identification, this work modifies the spinel-type model by removing cation mixing between Li and Co sites, due to insufficient resolution in the data to observe this level (<6%) of mixing. Reflections associated with each $LiCoO_2$ phase show changes as a function of charge or discharge and highlight that both phases are involved in the Li insertion/extraction process. Furthermore, changes in the reflections of these phases (*e.g.*, splitting) indicate that they also undergo phase transitions during the charge–discharge cycle of the battery.

3.2.1. *Layered $LiCoO_2$*

A number of studies have investigated the phase transitions in layered $LiCoO_2$ during electrochemical cycling [21,35,40–42,44,46–48]. The general process upon charging to 4.2 V is thought to follow: (i) a discharged state of $LiCoO_2$ to $Li_{0.93}CoO_2$ which is a single-layered phase region [21], termed 'I'; (ii) a first-order phase transition consisting of the co-existence of two layered phases, one of which is Li-rich or the phase I and the other a Li-poor (de-lithiated) version of the same phase, termed 'II', with a composition between $Li_{0.93}CoO_2$ and $Li_{0.75}CoO_2$ that corresponds to a voltage plateau of 3.9 V in a $LiCoO_2$/Li cell; (iii) a single-phase region between $Li_{0.75}CoO_2$ and $Li_{0.5}CoO_2$ corresponding to the Li poorer phase II which remains layered with a hexagonal setting; (iv) a disorder to order transition that leads to a monoclinic phase [49] with a small stability window around $Li_{0.5}CoO_2$, termed 'III'.

The splitting of the (0 0 3) reflection characteristic of the first-order phase transition [21,42] (*e.g.*, I → I + II → II) is shown in Fig. 2. Two-phases co-exist at 3.9 V with a corresponding plateau in the charging process lasting for 600 min. The two-phase region transforms to a single-layered phase (II). The behaviour of the (1 0 4) and (1 0 5) Bragg reflections close to the charged 4.2 V state of the battery is shown in Fig. 3, which corresponds to the formation of a monoclinic phase around $Li_{0.5}CoO_2$ [21,42,49]. To attain the equilibrium state of the battery, the 4.2 V charged state should have been maintained for a longer period of time or cycled potentiostatically (constant voltage), therefore this study is not able to discern completely the splitting of the (1 0 4) Bragg peak. Nevertheless, an intensity reduction is evident and the (1 0 5) Bragg peak shown in Fig. 3 clearly shows splitting and thereby provides evidence for the existence of the monoclinic phase. These data suggest the final Li content in the layered phase tested here is close to $x = 0.5$ in Li_xCoO_2 by comparing the phase transitions and voltages with trends and values reported in the literature [21,35,40–42,44,46–48]. These observations correlate with the *in situ* XRD work undertaken by Reimers and Dahn [21] and the various transitions are labelled using a similar notation with I, II and III in the bottom strip of Fig. 3. The variation in Li content for layered $LiCoO_2$ is used as a benchmark for the other phases.

3.2.2. *Spinel-type $LiCoO_2$*

In thin films, the transition from hexagonal $LiCoO_2$ to cubic spinel $LiCoO_2$ has been observed by means of *in situ* Raman spectroscopic analysis during laser irradiation [50]. The most convincing data showing the existence of spinel-type phases with electrochemical cycling is derived from *ex situ* transmission electron microscopy (TEM) studies [43,45]. These data are focused on particles of HT-$LiCoO_2$ before and after cycling, and show the formation of a cubic spinel phase. These authors suggest that part of the capacity fade of $LiCoO_2$-cathode batteries is due to the irreversible formation of the electrochemically less active spinel-type $LiCoO_2$ phase [43–45,50]. This is similar to the formation of cubic $LiNiO_2$ in the $LiNiO_2$ cathode [47]. They also predict spinel-type $LiCoO_2$ will be formed on charging the battery close to or slightly over 4.2 V. This voltage corresponds to the composition of the cathode as $Li_{0.5}CoO_2$ where stable spinel-type and layered-type phases can co-exist or form. The presence of the spinel-type phase is indicated in Fig. 4 through changes in the 2θ-value of a peak associated with this phase. This work presents the first evidence of Li insertion/extraction into/from a spinel-type $LiCoO_2$ phase in a $LiCoO_2$-cathode battery with electrochemical cycling. Furthermore, a series of phase transitions associated with the spinel-type $LiCoO_2$ phase as the battery is cycled are noted. Notably, the series of phase transitions associated with spinel-type $LiCoO_2$ is different to the phase transitions of the layered phase (top bars of Fig. 4).

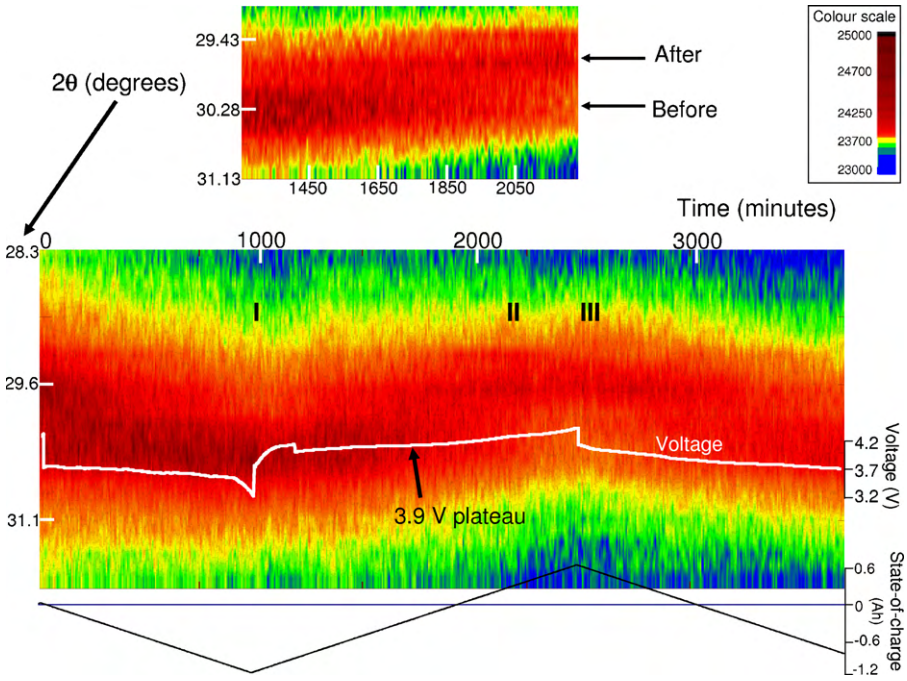

Fig. 2. First-order phase transition in layered $LiCoO_2$ at 3.9 V as illustrated by (0 0 3) peak with colour scale indicating intensity variations. Note, top image shows transition at first 3.9 V plateau and another transition seen at just over 3000 min. Transition takes approximately 600 min corresponding to change in Li content of $Li_{1-x}CoO_2$ of $0.25 \leq x \leq 0.07$ [21]. In the top image, (0 0 3) peak is seen at $2\theta = 30.28^\circ$ before transition and at $2\theta = 29.65^\circ$ after the transition. Superimposed white line shows voltage of battery and black line shows state-of-charge. Representative single-phase regions labelled 'I', 'II', and 'III'. (For interpretation of the references to colour in this figure legend, the reader is referred to the web version of the article.)

Assuming the charged state of the battery corresponds to a composition of around $Li_{0.5}CoO_2$, as observed in layered $LiCoO_2$, then this state is the ideal composition for spinel-type $LiCoO_2$ (the composition '$Li_{0.5}CoO_2$' represents the ideal spinel structure, $LiCo_2O_4$). Using Li contents in layered $LiCoO_2$ as a benchmark, as discharge occurs from spinel-type $Li_{0.5}CoO_2$ the following occurs. First, Li is incorporated in the spinel structure until ~$Li_{0.9}CoO_2$ (labelled 'A' in Fig. 4), which corresponds to the decrease in 2θ-values of the spinel-type reflection shown in Fig. 4. Second, once no more Li can be stably incorporated into the spinel-type structure characterised by A, a two-phase region occurs between ~$Li_{0.9}CoO_2$ and ~$Li_{0.95}CoO_2$ represented by 'A + B' (Fig. 4), where 'B' is a phase derived from spinel-type $LiCoO_2$ but not necessarily a spinel. The two-phase region is shown by the formation of a new Bragg peak at $2\theta = 76^\circ$,

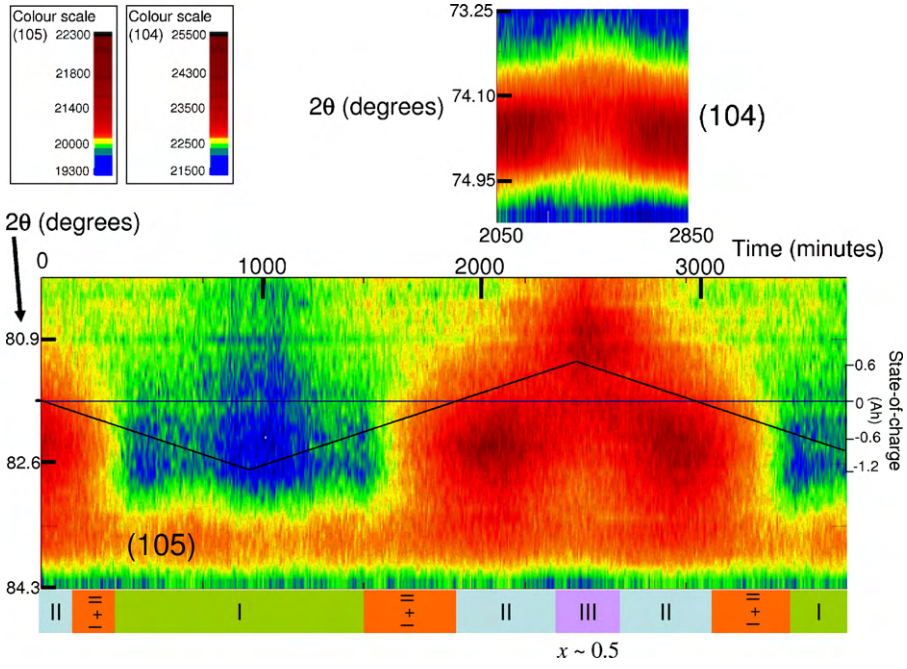

Fig. 3. Behaviour of (1 0 4) top and (1 0 5) bottom Bragg reflections with colour scale representing intensity variations. (1 0 5) reflection used to describe phase transitions of layered $LiCoO_2$. Lower strip shows different phases present using the notation I, II, and III. Superimposed black line shows state-of-charge of battery. (For interpretation of the references to colour in this figure legend, the reader is referred to the web version of the article.)

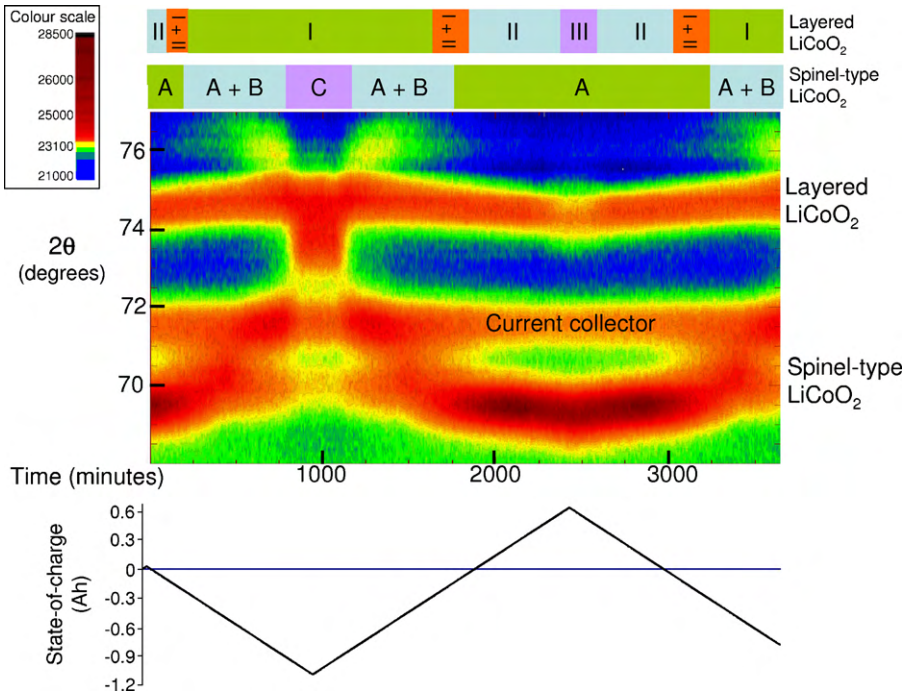

Fig. 4. ND patterns with state-of-charge of battery (black line). Reflections characteristic of various phases are labelled and colour scale illustrates intensity variation. Phase transitions of spinel-type and layered $LiCoO_2$ phases are described by bars at top. (For interpretation of the references to colour in this figure legend, the reader is referred to the web version of the article.)

which is related to phase B, and the large change in the intensity for the peak at $2\theta = 70^\circ$ phase A. Third, and finally, a single-phase region appears from $\sim Li_{0.95}CoO_2$ to $\sim LiCoO_2$ (derived from spinel-type) represented by region 'C' in Fig. 4. Note there is some peak overlap between the spinel-type, its derivative phases and other phases, *i.e.*, layered-type $LiCoO_2$ and Cu phases. The cycleability of the spinel-type $LiCoO_2$ and reproducibility of the phase transitions associated with Li insertion and extraction is shown by the two-phase region re-appearing on discharge just above 3500 min (Fig. 4).

The cathode prior to electrochemical cycling is composed entirely of layered $LiCoO_2$ and transforms to the spinel-type phase or one of its derivatives. Note that the *in situ* data do not show this layered to spinel transition. Determination of accurate cation distributions in the spinel-type phase and its derivatives requires the production of a sufficient quantity of the multiple intermediate phases and the execution of high-resolution *ex situ* ND experiments. Therefore, derivation of the details of the mechanism of this transformation (*e.g.*, on the surface of the cathode or in the first charge–discharge cycle) is beyond the scope of this study.

The difficulty of detecting *quasi*-spinel LT-$LiCoO_2$ using either ND or XRD data and its poorer electrochemical performance when compared with HT-$LiCoO_2$ has been reported elsewhere [38,39]. The presence of layered and spinel-type $LiCoO_2$ is clearly shown here and suggests that the spinel-type phase in this work is akin to ideal spinel (LiM_2O_4, where M = transition metal) rather than the *quasi*-spinel LT-$LiCoO_2$. The efficiency of electrochemical cycling of the spinel-type phase cannot be determined from these data. If the spinel-type phase is less efficient than the layered phase, the slow increase in the phase fraction of the spinel-type phase may be responsible for the performance degradation of the battery. Note, other factors can contribute to capacity fade such as microstructure, particle surfaces [45], Co dissolution [22], the surface of the graphite anode [46], and a gradual increase in the solid|electrolyte interface (SEI) layer [3]. Ideally, the first cycle for any battery should be performed with an *in situ* ND experiment and compared with later cycles.

3.3. Anode

In the discharged state of the battery, the anode is composed of graphite, *i.e.*, stacked graphene sheets along the *c*-axis adopting hexagonal $P6_3/mmc$ symmetry [51]. The 2θ-value of the (0 0 2) reflection (Fig. 5) decreases during charging as Li is inserted between graphene layers of graphite to form lithiated graphite. In the charged state of the battery (4.2 V), stoichiometric LiC_6 and lithiated graphite are present as shown by the splitting of the (0 0 2) graphite reflection (Fig. 5). A fraction of the anode is transformed to LiC_6 with charging and this fraction is transformed back to lithiated graphite with discharging. Hence, the anode shows the existence of a two-phase region whose behaviour is correlated with the charged state of the battery.

At the final stages of battery discharge, a sharp increase in the 2θ-value of the (0 0 2) lithiated graphite reflection results on the formation of de-lithiated graphite. During the initial stages of charging from the discharged state, a similarly sharp decrease in the 2θ-value of the (0 0 2) graphite reflection is noted and is associated with the formation of lithiated graphite. Significantly, the (0 0 2) reflection has relatively stable 2θ-values that correspond to lithiated graphite except near the discharged and charged states of the battery. Therefore, the lithiated graphite that is formed does not feature linear or large crystallographic changes with charging or discharging until the last stages of these electrochemical processes. These minimal crystallographic changes observed for lithiated graphite correspond to some regions of constant cell voltage.

To propose a mechanism for the behaviour of the anode, it should be noted that the above observations are obtained from galvanostatic measurements and are sensitive to bulk crystalline structures. No clear evidence for staged Li insertion into graphite [3,26,27] is observed. The formation of LiC_6 does show that the maximum Li content in graphitic anodes [3] is achieved. This work proposes that the SEI layer, which forms on the surface of the graphite anode after the first cycle and accounts for part of the

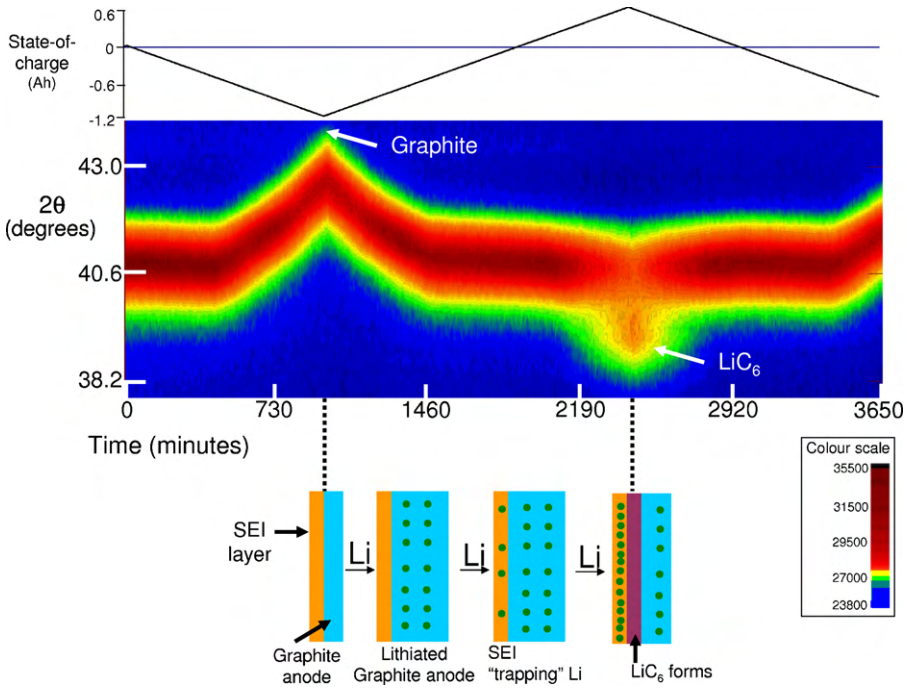

Fig. 5. ND patterns of (0 0 2) graphite reflection and state-of-charge (top) with colour scale representing reflection intensity. Splitting and formation of stoichiometric LiC_6 is shown near charged state of battery. Pure graphite (de-lithiated) exists where labelled. Graphical representation of proposed mechanism of Li insertion into anode correlated to time scale of diffraction patterns during charge (bottom), graphite is blue, SEI layer is orange, Li is green and LiC_6 purple. At discharged state, pure graphite and SEI layer comprise anode. With charging, Li is inserted into graphite, followed by insertion into SEI layer. At final stages of charging, there is sufficient Li in anode to form LiC_6. (For interpretation of the references to colour in this figure legend, the reader is referred to the web version of the article.)

charge and capacity loss [3,46], plays an integral role in trapping Li-ions. The initial stages of charging involve Li insertion into the de-lithiated graphite anode and correspond to a fall in the (0 0 2) reflection 2θ-values and an increase in cell voltage. Further charging produces a stable lithiated graphite phase (see Fig. 5). It is energetically feasible for Li-ions to build up near the surface of the anode or in the SEI layer rather than moving further into the anode. This work proposes that a build-up of Li-ions in the SEI layer results in the constant (0 0 2) reflection 2θ-values and regions of constant cell voltage. With continued charging, a fraction of the lithiated graphite at the interface becomes fully lithiated to form LiC_6 and increases the cell voltage. This continues as more of the lithiated graphite transforms to LiC_6 and results in a two-phase mixture of LiC_6 and lithiated graphite at the charged state of the battery. Upon discharge, Li-ions are released first from LiC_6 and are then followed by the trapped Li-ions in the SEI layer. This process results in only small changes in the lithiated graphite (0 0 2) reflection 2θ-values and cell voltage. Once trapped Li ions are released, the remaining Li ions that were inserted in the anode are extracted and cause a rapid increase in the (0 0 2) reflection 2θ-value and a drop in cell voltage. These observations are supported by the graphitic structural cell parameters and anodic phase fractions described in the refinements section. A review [3] on insertion compounds suggests anodic and SEI processes are likely to be quite complex and the above procedure is only an example of a possible mechanism.

3.4. Rietveld analysis

Qualitative observations have been used to describe structural behaviour of all of the phases found to exist in this battery. In order to provide further support for these observations, multi-phase sequential Rietveld refinement of structural models for the phases using the ND data have been undertaken. It is important to note that these refinements are significantly constrained and the information derived from them is considered with respect to factors such as: the data quality (Fig. 1(b)) which does not have sufficient resolution for precise structural solutions; the presence of multiple phases; the various phase transitions of these phases; background contributions from H-containing compounds; and the lack of structural information available in the literature for some derivative phases found in this work. In the refinements, the feature at $2\theta = 78^\circ$ (arising from the sample geometry) in Fig. 1(b) is excluded. The refined parameters are divided into two groups. The first group contains parameters that are refined for one dataset and fixed such as: (i) the profile function for each phase; (ii) isotropic atomic displacements parameters (ADPs) for Co, O, C and Cu atoms in each phase that are constrained to be the same between atom types; (iii) Li isotropic ADPs that are constrained to be the same between all Li-containing phases. The second group of parameters are allowed to refine throughout the charge–discharge cycle of the battery, these are: the background which was modelled using a shifted Chebyschev function with four terms, scale factors for each phase, and structural cell parameters for each phase except Cu (as the current-collector is not expected to show structural changes during the electrochemical process).

As stated in the introduction, ND is more sensitive to Li occupancies compared with XRD, but in this case there are up to five phases present in the structural refinements depending on the state-of-charge of the battery and Li is distributed among four of these phases. Each of the four Li-containing phases undergo a series of phase transitions, making refinement of Li occupancy not possible, and fixed Li occupancy is used. Incorporating the phase transitions into the refinements is difficult, due to the lack of structural information (*e.g.*, space-group symmetry and atomic positions) available in the literature. Furthermore, these data are not of sufficient resolution to solve a starting structural model for the essentially unknown de-lithiated phases. To account for the phase transitions the following procedures are used. For layered $LiCoO_2$, a single phase in a hexagonal setting is used throughout the refinements, since peak splitting in the two-phase region is small a

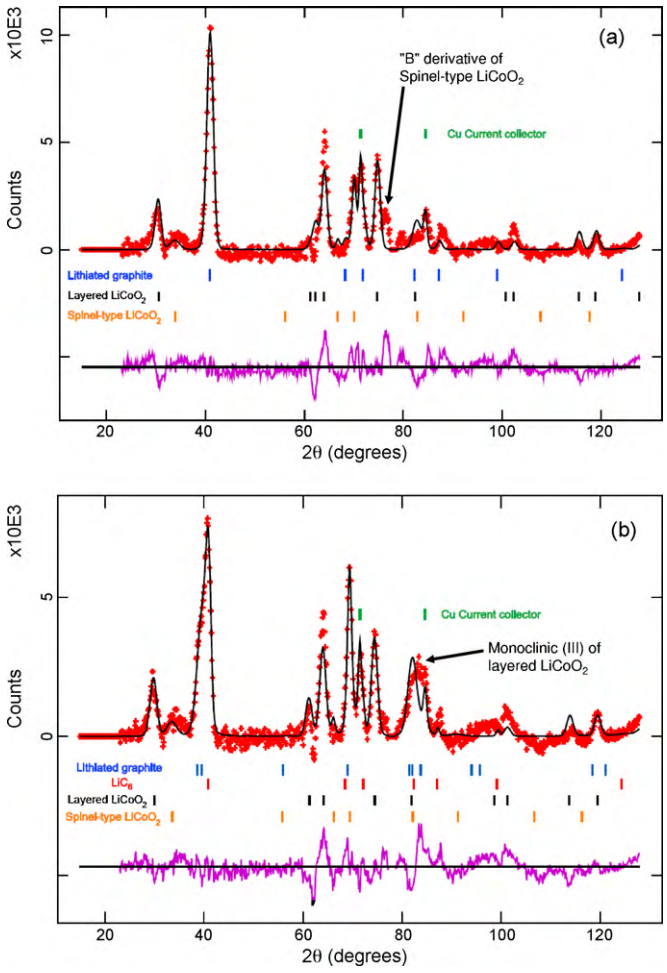

Fig. 6. Rietveld-refined models of ND patterns during *in situ* measurements near the (a) discharged and (b) charged state of the battery. Observed data shown as crosses (+), calculated data as solid line, and difference as solid line below.

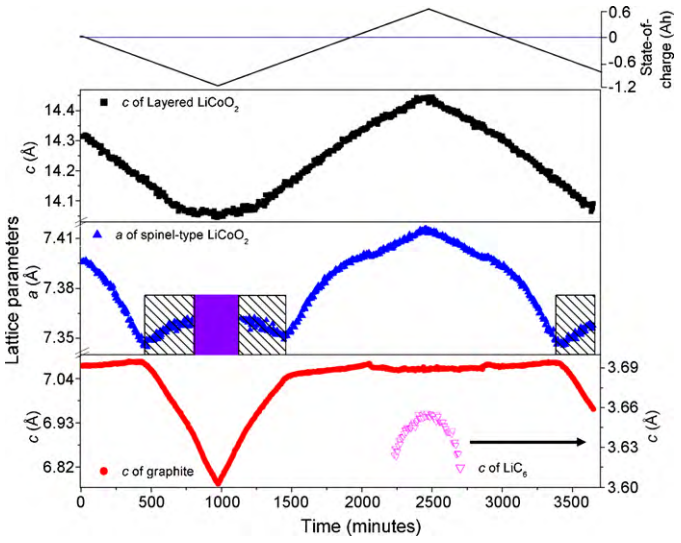

Fig. 7. Variation of selected lattice parameters of layered $LiCoO_2$ (black squares), spinel-type $LiCoO_2$ (blue triangles), graphite (red circles) and LiC_6 (magenta open triangles) as function of state-of-charge (top). In spinel-type $LiCoO_2$, two-phase region (A + B) has been shown with diagonal slashes as these lattice parameters are representative of only one phase (A), and single-phase region near discharged state is depicted by a purple box since structural solution not possible. (For interpretation of the references to colour in this figure legend, the reader is referred to the web version of the article.)

single peak approximated this behaviour. For spinel-type $LiCoO_2$, a single cubic phase (A) is used and is refined into a two-phase region (A + B) accounting for one (A) of these phases. The other phases derived from spinel-type $LiCoO_2$, B and C are not well determined in the literature, and since no starting structural model is available these are not incorporated into the refinements.

Rietveld-refined models of ND patterns are shown in Fig. 6 at two states of charge, highlighting contributions from the phases used. The phases and refined lattice parameters near the discharged state (Fig. 6(a)) or 1500 min, are layered $LiCoO_2$ with $a = 2.812(1)$ Å, $c = 14.173(8)$ Å, cubic spinel-type $LiCoO_2$ $a = 7.353(3)$ Å, and hexagonal lithiated graphite $a = 2.509(3)$ Å, $c = 7.049(2)$ Å. The statistics of this refinement are $wR_p = 2.06\%$, $R_p = 1.53\%$ and $\chi^2 = 8.17$ for 13 variables. Note for the spinel-type $LiCoO_2$, this is a two-phase region (A + B) and a key reflection of the derivative B phase is observed. The phases and refined lattice parameters near the charged state (Fig. 6(b)), or 2325 min are layered $LiCoO_2$ with $a = 2.805(1)$ Å, $c = 14.400(9)$ Å, cubic spinel-type $LiCoO_2$ $a = 7.419(2)$ Å, hexagonal lithiated graphite $a = 2.503(3)$ Å, $c = 7.059(4)$ Å, and hexagonal LiC_6 $a = 4.227(26)$ Å, $c = 3.626(6)$ Å. The statistics of this refinement are $wR_p = 1.90\%$, $R_p = 1.41\%$ and $\chi^2 = 6.93$ for 16 variables. In general, fits of the Rietveld-refined model to the diffraction patterns are reasonable, with wR_p values between 2 and 4%, R_p between 1 and 3%, and χ^2 ranging from 6 to 11, for a maximum of 16 independent refinable parameters. These statistics and refinements should be considered in light of the difficult experimental conditions stated above, particularly the significant background contributions and the uncertainty in the exact Li concentrations of the Li-containing phases.

The variation in the lattice parameters as a function of cycling is shown in Fig. 7. Similar trends (*e.g.*, increasing or decreasing) of the *c* lattice parameter of layered $LiCoO_2$ and the lattice parameter of cubic spinel-type $LiCoO_2$ is seen during cycling and this indicates that these phases are undergoing a concerted Li insertion and extraction process with discharge–charge. Note only a small variation in the *a* lattice parameter of the layered $LiCoO_2$ phase [21] is observed, since Li is inserted/extracted from sites between negatively charged CoO_2 layers that are arranged along the *c*-axis. This observation is consistent with the location of both $LiCoO_2$ phases at the cathode in agreement with Ref. [22] where no evidence for electrophoresis of $LiCoO_2$ to the anode was observed. The difference in the Li insertion/extraction mechanism, and in turn the cycling efficiency, of the two $LiCoO_2$ structures is indicated by the different rates of change in the lattice parameters during cycling. As the battery is charged, $LiCoO_2$ is transformed to $Li_{0.5}CoO_2$ and the *c* lattice parameter of layered $LiCoO_2$ was shown to increase by ~3% by Kim et al. [48]; data analysed in this study show an increase of 2.9%. The spinel-type $LiCoO_2$ in the single-phase domain (A) increases by less than 1% this highlights the different affects on the lattice with Li extraction. The largest increase is shown by the graphite *c* lattice parameter, 4.3%, but most of this increase is concentrated near the discharged state (Fig. 7), corresponding to the initial insertion of Li into the de-lithiated graphite structure and the changes in the 2θ-value of (0 0 2) graphite reflection described above (Fig. 5).

Ideally, phase fractions as a function of electrochemical cycling would provide further insight into the mechanisms of the battery. Unfortunately, both the inability to refine the Li concentrations and the overlap of reflections from the spinel-type $LiCoO_2$ and Cu reflections (an internal standard) meant analysis of phase fractions was unreliable near the discharged state of the battery. The phase fractions of the crystalline components comprising the anode near the charged state of the battery were determined, as shown in Fig. 8. At the maximum applied voltage of 4.2 V, about 64% of the anode transforms into LiC_6 and the remainder remains as lithiated graphite. This result agrees with the mechanism of Li

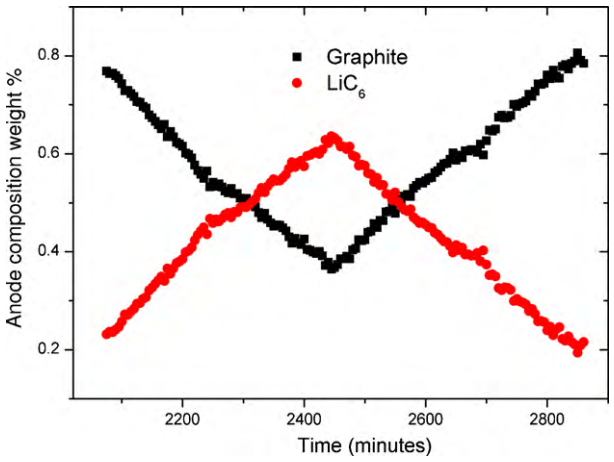

Fig. 8. Phase fractions of crystalline lithated graphite and LiC_6 near charged state of battery. Note these phase fractions begin with LiC_6 comprising more than 20% of anode, as there is no means to incorporate LiC_6 at lower concentrations due to peak overlap with lithiated graphite.

insertion/extraction into/from the anode proposed above. Note, the derived phase fractions are also limited by the constraints and data quality issues described above.

3.5. Future neutron diffraction experiments

Note that the statistics from the Rietveld refinements have to be judged with respect to the quality of fit and the underlying crystallographic properties of the materials being discussed. The R_p and wR_p values are consistent with good quality refinements against ND data. The goodness-of-fit term, χ^2, is higher than the optimum value mainly due to the fitting of the background which can be seen to be poorly approximated at high angles (Fig. 6). The phases that were used in these refinements are not sufficient to model certain regions in the ND patterns where two-phase regions of compounds co-existed, *e.g.*, A + B for spinel-type $LiCoO_2$. Therefore, conclusions drawn from this study are based on observations in diffraction patterns and supported by the lattice parameter fluctuations in the refinements rather than based on details in the structural refinements.

In order to improve future *in situ* ND experiments, the background generated from the hydrogen-containing electrolyte needs to be significantly reduced. This can be achieved by either reducing the quantity of electrolyte used, which would affect the performance of the battery, or by replacing the electrolyte with deuterated versions. To improve the modelling of peak shapes and to remove other sample geometry effects, a cylindrical battery should be used. It is also important to optimise the electrochemical properties and timing for electrochemical cycling (*e.g.*, applied current) before performing an *in situ* ND experiment, since allocated time on neutron diffraction instruments is limited. Ideally, *in situ* ND data should be collected for 2–3 full cycles. Anomalies that are not related to bulk crystallographic changes in the electrode materials cannot be determined directly from *in situ* ND, *e.g.*, the small drop in voltage during charging at 1200 min, observed in Fig. 2.

4. Conclusions

The results of an *in situ* ND study of a commercially available $LiCoO_2$/C battery are presented. Crystalline structures in the entire battery are probed over ~1.5 charge–discharge cycles. In the cathode, both a layered $LiCoO_2$ and cubic spinel-type $LiCoO_2$ are found to exist. These phases have Li inserted and extracted into/from them with electrochemical cycling and this is shown by changes in their respective lattice parameters. Each of the $LiCoO_2$ phases undergoes a series of phase transitions described by $I \rightarrow I + II \rightarrow II \rightarrow III$ for layered $LiCoO_2$ while charging (losing Li) and $C \rightarrow A + B \rightarrow A$ for spinel-type $LiCoO_2$ while charging. This is the first report of Li insertion/extraction in the spinel-type phase with electrochemical cycling in a battery and thus the first observation of the phase transitions involved in this phase with cycling. The gradual build-up of the spinel-type phase may lead to capacity fading in these batteries, but other factors can play a significant role.

In the anode, near the charged state of the battery there exists both lithiated graphite and LiC_6. Near the discharged state of the battery and moving from discharging to charging, a rapid decrease followed by increase in the *c* lattice parameter of lithiated graphite is seen. At stages when the battery is at constant voltage, the *c* lattice parameter of lithiated graphite is stable. A mechanism for this observation is proposed and further work will be directed at understanding this behaviour of graphitic anodes.

In one succinct measurement, this study is able to re-produce the findings of the large amount of work undertaken separately on $LiCoO_2$ electrodes and graphite based anodes, as well as generating new insights into the complex behaviour of charging/discharging batteries.

Acknowledgements

Dr. Kamarulzaman would like to thank the Universiti Technologi MARA and ANSTO for travel funding. The authors are also grateful to the Academy of Science, Malaysia (grant no. P.20c), CLEON Technologies Sdn Bhd, Dr. R. Subban, Dr. N. Kamarudin and Dr. M. Bustam for supporting this project.

References

[1] J.-M. Tarascon, M. Armand, Nature 414 (2001) 359–367.
[2] T. Nagaura, K. Tozawa, Prog. Batteries Solar Cells 9 (1990) 209.
[3] M. Winter, J.O. Besenhard, M.E. Spahr, P. Novak, Adv. Mater. 10 (1998) 725–763.
[4] J.B. Goodenough, Y. Kim, Chem. Mater. 22 (2009) 587–603.
[5] M. Wakihara, Mater. Sci. Eng. R 33 (2001) 109–134.
[6] N. Kamarulzaman, R. Yusoff, N. Kamarudin, N.H. Shaari, N.A. Abdul Aziz, M.A. Bustam, N. Blagojevic, M. Elcombe, M. Blackford, M. Avdeev, A.K. Arof, J. Power Sources 188 (2009) 274–280.
[7] C. Baehtz, Th. Buhrmester, N.N. Bramnik, K. Nikolowski, H. Ehrenberg, Solid State Ionics 176 (2005) 1647–1652.
[8] C. Lampe-Onnerud, J.O. Thomas, M. Hardgrave, S. Yde-Anderse, J. Electrochem. Soc. 142 (1995) 3648–3651.
[9] Y. Sato, T. Asada, H. Tokugawa, K. Kobayakawa, J. Power Sources 68 (1997) 674–679.
[10] M.R. Palacin, G.G. Amatucci, M. Anne, Y. Chabre, L. Seguin, P. Strobel, J.-M. Tarascon, G. Vaughan, J. Power Sources 81 (1999) 627–631.
[11] B. Gerand, A. Blyr, A. Du Pasquier, J.B. Leriche, L. Seguin, J. Power Sources 81 (1999) 922–924.
[12] M. Balasubramanian, X. Sun, X.Q. Yang, J. McBreen, J. Power Sources 92 (2001) 1–8.
[13] W.S. Yoon, N. Kim, X.Q. Yang, J. McBreen, C.P. Grey, J. Power Sources 119 (2003) 649–653.
[14] K.W. Nam, W.S. Yoon, H. Shin, K.Y. Chung, S. Choi, X.Q. Yang, J. Power Sources 192 (2009) 652–659.
[15] P.Y. Liao, J.G. Duh, J.F. Lee, H.S. Sheu, Electrochem. Acta 53 (2007) 1850–1857.
[16] J. McBreen, J. Solid State Electrochem. 13 (2009) 1051–1061.
[17] W.S. Yoon, K.Y. Chung, J. McBreen, X.Q. Yang, Electrochem. Commun. 8 (2006) 1257–1262.
[18] W. Wen, B. Kumarasamy, S. Mukerjee, M. Auinat, Y. Ein-Eli, J. Electrochem. Soc. 152 (2005) A1902–A1911.
[19] S.T. Myung, S. Komaba, N. Hirosaki, N. Kumagai, K. Arai, R. Kodama, I. Nakai, J. Electrochem. Soc. 150 (2003) A1560–A1568.
[20] M.A. Rodriguez, M.R. Keenan, G. Nagasubramanian, J. Appl. Cryst. 40 (2007) 1097–1104.
[21] J.N. Reimers, J.R. Dahn, J. Electrochem. Soc. 139 (1992) 2091–2096.
[22] G.G. Amatucci, J.-M. Tarascon, L.C. Klein, Solid State Ionics 83 (1996) 167–173.
[23] F. Rosciano, M. Holzapfel, W. Scheifele, P. Novak, J. Appl. Cryst. 41 (2008) 690–694.
[24] O. Bergstom, A.M. Andersson, K. Edstrom, T. Gustafsson, J. Appl. Cryst. 31 (1998) 823–825.
[25] H. Berg, H. Rundlov, J.O. Thomas, Solid State Ionics 144 (2001) 65–69.
[26] M.A. Rodriguez, D. Ingersoll, S.C. Vogel, D.J. Williams, Electrochem. Solid-State Lett. 7 (2004) A8–A10.

[27] M.A. Rodriguez, M.H. Van Benthem, D. Ingersoll, S.C. Vogel, H.M. Reiche, Powder Diffr. 25 (2010) 143–148.
[28] Z.P. Guo, G.D. Du, Y. Nuli, M.F. Hassan, H.K. Liu, J. Mater. Chem. 19 (2009) 3253–3257.
[29] S. Vivet, M. Latroche, Y. Chabre, J.-M. Joubert, B. Knosp, A. Percheron-Guegan, Physica B 362 (2005) 199–207.
[30] A.J. Studer, M.E. Hagen, T.J. Noakes, Physica B 385–386 (2006) 1013–1015.
[31] D. Richard, M. Ferrand, G.J. Kearley, J. Neutron Res. 4 (1996) 33–39.
[32] A.C. Larson, R.B. Von Dreele, General Structure Analysis System (GSAS), Los Alamos National Laboratory Report LAUR 86-748, 1994.
[33] B.H. Toby, J. Appl. Cryst. 34 (2001) 210–213.
[34] M. Douin, L. Guerlou-Demourgues, M. Menetrier, E. Bekaert, L. Goubault, P. Bernard, C. Delmas, J. Solid State Chem. 182 (2009) 1273–1280.
[35] G.G. Amatucci, J.-M. Tarascon, L.C. Klein, J. Electrochem. Soc. 143 (1996) 1114–1123.
[36] E. Rossen, J.N. Reimers, J.R. Dahn, Solid State Ionics 62 (1993) 53–60.
[37] R.J. Gummow, M.M. Thackeray, W.I.F. David, S. Hull, Mater. Res. Bull. 27 (1992) 327–337.
[38] R.J. Gummow, D.C. Liles, M.M. Thackeray, W.I.F. David, Mater. Res. Bull. 28 (1993) 1177–1184.
[39] R.J. Gummow, D.C. Liles, M.M. Thackeray, Mater. Res. Bull. 28 (1993) 235–246.
[40] E. Antolini, Solid State Ionics 170 (2004) 159–171.
[41] M. Yoshio, H. Tanaka, K. Tominaga, H. Noguchi, J. Power Sources 40 (1992) 347–353.
[42] T. Ohzuku, A. Ueda, J. Electrochem. Soc. 141 (1994) 2972–2977.
[43] R. Yazami, Y. Ozawa, H. Gabrisch, B. Fultz, Electrochim. Acta 50 (2004) 385–390.
[44] H. Wang, Y.-I. Jang, B. Huang, D.R. Sadoway, Y.-M. Chiang, J. Electrochem. Soc. 146 (1999) 473–480.
[45] H. Gabrisch, R. Yazami, B. Fultz, J. Power Sources 119–121 (2003) 674–679.
[46] X. Wang, Y. Sone, G. Segami, H. Naito, C. Yamada, K. Kibe, J. Electrochem. Soc. 154 (2007) A14–A21.
[47] Y.-M. Choi, S.-I. Pyun, J.-S. Bae, S.-I. Moon, J. Power Sources 56 (1995) 25–30.
[48] Y.J. Kim, E.-K. Lee, H. Kim, J. Cho, Y.W. Cho, B. Park, S.M. Oh, J.K. Yoon, J. Electrochem. Soc. 151 (2004) A1063–A1067.
[49] Y. Takahashi, N. Kijima, K. Tokiwa, T. Watanabe, J. Akimoto, J. Phys.: Condens. Matter 19 (2007) 436202.
[50] S.W. Song, K.S. Han, H. Fujita, M. Yoshimura, Chem. Phys. Lett. 344 (2001) 299–304.
[51] A.W. Hull, Ber. Dtsch. Chem. Ges. 59 (1926) 2433–2444.

Glossary

SoC: state-of-charge
XRD: X-ray diffraction
ND: neutron diffraction
D: deuterium
d: interplanar spacings
OPAL: Open Pool Australian Light-water reactor
ANSTO: Australian Nuclear Science and Technology Organisation
CIF: crystallographic information files
ICSD: Inorganic Crystal Structure Database
HT-$LiCoO_2$: high-temperature $LiCoO_2$
LT-$LiCoO_2$: low-temperature $LiCoO_2$
TEM: transmission electron microscopy
SEI: solid|electrolyte interface
ADPs: atomic displacements parameters
R_p and wR_p: R-factors or statistical residuals for quality of minimisation of refined model against collected data
χ^2: goodness-of-fit term